

Supplementary Materials

Pectin chemistry and cellulose crystallinity govern pavement cell morphogenesis in a multi-step mechanism

Bara Altartouri, Amir J Bidhendi, Tomomi Tani, Johnny Suzuki, Christina Conrad, Youssef Chebli, Na Liu, Chithra Karunakaran, Giuliano Scarcelli and Anja Geitmann

Supplementary Note 1: Distinction between true lobes and tricellular junctions

Pavement cells have two types of protrusions that are generated by entirely different processes. Tricellular junctions are formed through the deposition of a dividing wall during cytokinesis (Supplemental Fig. S2A), whereas undulations in an existing wall segment are formed through the processes discussed in the present paper. Although they resemble lobes, tricellular junctions were therefore excluded from the lobe count analyses. Recently developed automated lobe counting tools such as skeleton methods and lobe finder (Wu et al., 2016) do not distinguish between true lobes and tricellular junctions in pavement cells, but we consider this distinction crucial. Our choice is supported by the fact that including tricellular junctions in the lobe number count partially masks the difference between the *any1* mutant and the wild type (Supplemental Fig. S2, B and C). Thus, in this study, we focus exclusively on true lobes. To distinguish a true lobe from a straight cell border it had to have a curvature with the depth (Fig. 1G) of at least one pixel. In our study one pixel equals to 0.66 μm .

We opted for the terms lobe (also used by Fu et al. (2002), Panteris and Galatis (2005) and Zhang et al. (2011)) and neck (Fu et al., 2002; Fu et al., 2005) for ease of reading. Terms used by others include 'constriction' (Panteris and Galatis, 2005) 'indent' or 'indentation' (Fu et al., 2005) ('neck' in our terminology) and protrusion (Zhang et al., 2011) ('lobe' in our terminology). We avoid the terms 'convex' and 'concave' since they require a reference frame and might therefore lead to misunderstanding ('convex' is used by Zhang et al. (2011) to indicate a protrusion (lobe) using the cell as a reference, but by Armour et al. (2015) and Majda et al. (2017) to indicate an indent (neck) with the anticlinal wall as reference). We prefer to avoid all nomenclature related confusion while keeping the terms as intuitive as possible.

Supplementary Note 2: Calculating the longitudinal modulus

The Brillouin frequency shift (BFS) is related to the longitudinal modulus of material based on the following equation (Scarcelli and Yun, 2007; Scarcelli et al., 2015):

$$M' = \frac{\Omega^2 \lambda^2 \rho}{4n^2} \quad (\text{Eq.1})$$

Where M' is the longitudinal modulus, Ω is the BFS, λ is the optical wavelength, ρ is the material density, n is the refractive index. Importantly, the component of the modulus measured is along the direction of the incident laser beam, that is perpendicular to the periclinal wall and thus cellulose microfibrils. Here, we assumed the refractive index to be 1.1 g/cm³ and the density of the primary cell wall to be 1.41 (Elsayad et al., 2016). While density and refractive index may differ between lobe and neck regions because of the different abundance of cellulose microfibrils, in biological materials, it has been shown that the ratio between the two, ρ/n^2 , does not vary significantly. Therefore, BFS can be assumed to be directly related to the longitudinal modulus (Scarcelli et al., 2015; Elsayad et al., 2016).

Supplementary Note 3: Effect of cell geometry on the detected BFS

In Brillouin spectroscopy, one consequence of geometrical effects of the sample could be local variations in signal intensity that are not caused by the mechanical properties of the material but by its geometry. Brillouin shift is normally independent from signal intensity of Brillouin scattering. However, in the circumstance of a large loss in signal intensity, an artifact may be present only due to an inability to fit the Lorentzian function to the spectrum during post-processing. In the present study, to ensure that there was no substantial variation in signal intensity caused by pavement cell geometry, we quantitatively measured the Brillouin signal intensity corresponding to the neck and lobe ROIs. The difference in the signal intensity between the neck and the corresponding lobe of the same undulation was typically below 15 percent (Supplemental Figures S4B and C). Importantly, the data points did not show any bias for lobe or neck as they were evenly distributed above and below 0% difference.

Supplementary Materials and Methods

Microscopy and image acquisition

Three types of microscopy were used in this study. Confocal laser scanning microscopy (CLSM), polarized fluorescence microscopy (LC-POLScope; laboratory of Dr. Tomomi Tani, Marine Biological Laboratory) and Brillouin microscopy (laboratory of Dr. Giuliano Scarcelli, University of Maryland).

For CLSM a Zeiss LSM 510 LSM 5LIVE/Axiovert 200M system was used. The 5LIVE/Axiovert 200M system was used for shape metrics analysis and time-lapse of cortical microtubules. The 532-nm laser was used with an emission filter 590-625 nm to visualize the cell wall (labelled with PI). The 488-nm laser was used with emission filter 500-530 nm to visualize GFP-TUB6. The time-lapse images were acquired every 6 hours. 63x oil-immersion objective lens (NA = 1.4) was used for time-lapse of microtubules and 20x objective lens (NA = 0.8) was used for the shape metrics measurement.

The Instantaneous FluoPolScope (Mehta et al., 2016; Swaminathan et al., 2017) was used in this study to address the anisotropy of cellulose at subcellular regions (i.e. neck and lobe). The 561-nm laser (Coherent OBIS, 20mW) was used for the total internal reflection illumination through an oil-immersion objective lens (Nikon TIRF 60x, NA = 1.49) to image cellulose labelled with S4B. The side length of a single pixel of the images captured with a camera (Andor iXon+ EMCCD

camera) corresponds to 0.12 μm at the sample stage. A quadrant imaging system as described in (Mehta et al., 2016) was used for instantaneous analysis of fluorescence emission of cellulose-bound S4B along four polarization orientations at 45° increments. Back-ground corrected polarization-resolved fluorescence intensities ($I_0, I_{45}, I_{90}, I_{135}$) were used to compute polarized fluorescence orientation (θ) and the anisotropy of fluorescence polarization (p) per pixel as follows:

$$\theta = \tan^{-1} \frac{I_0 - I_{90}}{I_{45} - I_{135}} \quad (\text{Eq.2})$$

$$p = \frac{\sqrt{(I_0 - I_{90})^2 + (I_{45} - I_{135})^2}}{0.5 \times (I_0 + I_{45} + I_{90} + I_{135})} \quad (\text{Eq.3})$$

Brillouin microscopy was used to assess the stiffness of the periclinal wall of pavement cells. The detailed setup of the Brillouin microscopy can be found in our previous publications (Scarcelli and Yun, 2007, 2011). Briefly, a green laser of 532 nm with an optical power on the sample of 2.5 mW was used. The laser was focused onto the sample using an objective lens of 40x and a numerical aperture of 0.6. The resolution was 0.54 μm laterally (x-y) and 0.90 μm (z) axially. x-y sectional images were obtained by translating x-y motorized stage (Prior Scientific, Inc., Rockland, MA) with exposure time of 0.2 second. After epi-detection of the Brillouin scattering light, a two-stage VIPA spectrometer and an EMCCD camera (iXon Du-897; Andor, Belfast, Northern Ireland) were used to image the Brillouin frequency shifts. LABVIEW (National Instruments, Austin, TX) was used for system automatic control and the data acquisition.

For all image acquisition, samples were mounted between slide and cover slip for imaging. For the time-lapse imaging, samples were placed immediately back to the in vitro growth chamber following each image acquisition. ROIs were traced at each time point manually.

Image analysis

Cell shape metrics analysis was done with ImageJ software (<http://imagej.nih.gov/ij>). Maximum projections of z-stack images were used for the analysis. Cell outlines were traced manually. Area, perimeter, convex hull fit and circularity (4π (area/perimeter²)) were determined automatically for each cell by the ImageJ software. The lobe number was counted manually and represents all convex bends in the cell wall excluding those at tricellular junctions (Supplementary Note 1). The aspect ratio of the lobe represents the ratio of depth/width of the lobe. The width is the length of the tangent between the farthest points (troughs) of the lobe. The depth is the distance between the midpoint of the width and the tip of the lobe. Any curvature that has a width of at least one pixel (0.66 μm) was considered as a lobe. Data of the cell shape metrics at days 1, 2, 3, and 4 after germination were taken from different seedlings. Shape metrics data of 1 day after germination represent all the cells in the image excluding dividing cells and stomata. In order to exclude newly divided cells, the shape metrics data of 2, 3 and 4 days after germination considered all cells in an image that had an area above the smallest area value measured in the dataset of the previous day.

For all analyses, the tips of the lobe/neck regions were defined as follows. A straight line (reference line) was drawn as a tangent between the troughs of the lobe. The reference line was then shifted in parallel direction until it reached the farthest point of the lobe of interest. The point

was considered as the tip of the lobe. For the anisotropy of cortical microtubules, dynamics of demethyl-esterified pectin, cellulose alignment and the stiffness of the periclinal wall analysis, ROIs were selected as circular shapes with area of 4-9 μm^2 at the tip of lobe/neck region. Relative difference in the signal intensity between neck and corresponding lobe region equals (signal intensity at the neck region - signal intensity at the lobe region) / signal intensity at the neck region. To examine the temporal correlation between the dynamics of demethyl-esterified pectin and cortical microtubules at developing cell border curvatures, maximum projections of z-stacks were used. The cell border segment of interest was chosen based on the curvature at 18 H, and traced back to a straight segment at time 0. The circular ROI was placed on the neck side of the cell border at a (future) peak curvature and two identically sized ROIs were placed left and right on the same side of the border. The signal intensity of the central ROI was divided by the mean intensity signal of the two adjacent ROIs. Brightness and contrast adjustments were done on individual z-stack to ensure optimal contrast of microtubules and propidium iodide staining on the presented micrographs. For each image, the signal from unstained regions was considered as background signal for the analysis of microtubules and spatial occurrence of demethyl-esterified pectin. The average value of the background signal was subtracted from the fluorescence intensity value determined for the ROI. The grayscale of some fluorescence micrographs was inverted for better visualization. All quantitative analyses were done on the original grayscale fluorescence micrographs.

The FibrilTool plugin was developed to measure the orientation of fibrillar structures (i.e. cytoskeleton) in plant cells (Boudaoud et al., 2014). It was used in this study to determine the anisotropy of the cortical microtubules during the time-lapse analysis. Maximum intensity projections of z-stack images were used for the analysis. The curvature of the lobe during the time-lapse analysis was determined using Kappa, a Fiji plugin for curvature analysis.

To examine the cellulose alignment in the periclinal wall of the pavement cells, an optical section showing the periclinal wall of the ROI was used. The signal from unstained regions, for each image independently, was considered as a background signal. This value was subtracted from the signal value of the ROI. The anisotropy analysis was based on the fluorescence emission at the different angles (Eq.3). The mean orientation and anisotropy at each pixel were measured based on the variation of fluorescence intensity that was detected by different emission paths. A MATLAB code, RTFluorPolGUI developed by Dr. Shalin B. Mehta of the Marine Biological Laboratory, Woods Hole, USA (Mehta et al., 2016), was used to measure the fluorescence anisotropy of the cellulose stained with S4B at each pixel. Brightness and contrast adjustments were done on the presented micrographs.

For Brillouin scattering analysis, spectrum data acquired by the camera were fitted with the Lorentzian function to determine Brillouin frequency shifts. De-ionized water and the bottle glass with known Brillouin frequency shift were used for the calibrations of the frequency-pixel conversion ratio (GHz per pixel) and the free spectral range in our spectrometer. Before and after Brillouin measurement, fluorescence images of pavement cells were taken for the co-localization of the ROI. A defined region of the fluorescence image was further chosen for the Brillouin measurement. After the measurement, the fluorescence image of the cell wall and the Brillouin frequency shift image were aligned using ImageJ software. The grayscale value of each pixel in the Brillouin scattering image represents the frequency shift in the GHz. ROI at the tip of the neck/lobe regions was defined and the pixel values were recorded.

Tensile testing of hypocotyls

Dark-grown *Arabidopsis* hypocotyls (5 days after germination) of wild type and *any1* mutant were plasmolyzed with 0.8 M mannitol (Sigma-Aldrich) for 20 minutes. The mid-region of the etiolated hypocotyl was mounted on a custom-built tensile device between two gripping ends that were 4 mm separated from each other by a linear motorized stage (Thorlabs). The sample was kept moisturized by adding a drop of the mannitol solution. The force was measured by a micro load cell sensor attached to one of the gripping ends. The sensor used in this experiment was designed for forces up to 5 gf (0.049 N) allowing reliable measurement of forces as small as 10 μ gf (0.098 μ N). The sensor was calibrated against a series of known weights each time that the device was reconfigured. The displacement of the grips was measured with micrometer resolution by a linear variable displacement transducer (LVDT). The forces generated by sample stretch were collected at the PC and registered using a custom Python code. These force-displacement data were used to generate the stress-strain curves. The custom-built tensile device was used under a Zeiss Discovery V8 stereomicroscope, 0.63x and 8x zoom, to allow measuring the diameter of each sample to calculate the area of the hypocotyl cross section. The apparent Young's modulus was calculated from the slope in the elastic range of the stress-strain curve. The density of the cell wall material per cross section in wild type and mutant was not significantly different ($P > 0.05$) allowing direct comparison of the calculated apparent Young's moduli. The density was measured from 5 different patches of dry etiolated hypocotyls with known length and diameter for wild type and *any1* mutant. The average densities were $0.035 \text{ g/cm}^3 \pm 0.003$ (SE) and $0.034 \text{ g/cm}^3 \pm 0.004$ (SE) of wild type and *any1* mutant, respectively.

Literature cited

- Armour WJ, Barton DA, Law AM, Overall RL (2015) Differential growth in periclinal and anticlinal walls during lobe formation in *Arabidopsis* cotyledon pavement cells. *Plant Cell* 27: 2484-2500
- Boudaoud A, Burian A, Borowska-Wykret D, Uyttewaal M, Wrzalik R, Kwiatkowska D, Hamant O (2014) FibrilTool, an ImageJ plug-in to quantify fibrillar structures in raw microscopy images. *Nat Protoc* 9: 457-463
- Elsayad K, Werner S, Gallemi M, Kong J, Sanchez Guajardo ER, Zhang L, Jaillais Y, Greb T, Belkhadir Y (2016) Mapping the subcellular mechanical properties of live cells in tissues with fluorescence emission-Brillouin imaging. *Sci Signal* 9: rs5
- Fu Y, Gu Y, Zheng Z, Wasteneys G, Yang Z (2005) *Arabidopsis* interdigitating cell growth requires two antagonistic pathways with opposing action on cell morphogenesis. *Cell* 120: 687-700
- Fu Y, Li H, Yang Z (2002) The ROP2 GTPase controls the formation of cortical fine F-actin and the early phase of directional cell expansion during *Arabidopsis* organogenesis. *Plant Cell* 14: 777-794
- Fujita M, Wasteneys GO (2014) A survey of cellulose microfibril patterns in dividing, expanding, and differentiating cells of *Arabidopsis thaliana*. *Protoplasma* 251: 687-698
- Majda M, Grones P, Sintorn IM, Vain T, Milani P, Krupinski P, Zagorska-Marek B, Viotti C, Jonsson H, Mellerowicz EJ, Hamant O, Robert S (2017) Mechanochemical polarization of contiguous cell walls shapes plant pavement cells. *Dev Cell* 43: 290-304 e294

- Mehta SB, McQuilken M, La Riviere PJ, Occhipinti P, Verma A, Oldenbourg R, Gladfelter AS, Tani T (2016) Dissection of molecular assembly dynamics by tracking orientation and position of single molecules in live cells. *Proc Natl Acad Sci USA* 113: E6352-E6361
- Panteris E, Galatis B (2005) The morphogenesis of lobed plant cells in the mesophyll and epidermis: organization and distinct roles of cortical microtubules and actin filaments. *New Phytol* 167: 721-732
- Sampathkumar A, Krupinski P, Wightman R, Milani P, Berquand A, Boudaoud A, Hamant O, Jonsson H, Meyerowitz EM (2014) Subcellular and supracellular mechanical stress prescribes cytoskeleton behavior in *Arabidopsis* cotyledon pavement cells. *eLife* (Cambridge) 3: e01967
- Scarcelli G, Polacheck WJ, Nia HT, Patel K, Grodzinsky AJ, Kamm RD, Yun SH (2015) Noncontact three-dimensional mapping of intracellular hydromechanical properties by Brillouin microscopy. *Nat Methods* 12: 1132-1134
- Scarcelli G, Yun SH (2007) Confocal Brillouin microscopy for three-dimensional mechanical imaging. *Nat Photonics* 2: 39-43
- Scarcelli G, Yun SH (2011) Multistage VIPA etalons for high-extinction parallel Brillouin spectroscopy. *Opt Express* 19: 10913-10922
- Swaminathan V, Kalappurakkal JM, Mehta SB, Nordenfelt P, Moore TI, Koga N, Baker DA, Oldenbourg R, Tani T, Mayor S, Springer TA, Waterman CM (2017) Actin retrograde flow actively aligns and orients ligand-engaged integrins in focal adhesions. *Proc Natl Acad Sci USA* 114: 10648-10653
- Wu TC, Belteton SA, Pack J, Szymanski DB, Umulis DM (2016) LobeFinder: A convex hull-based method for quantitative boundary analyses of lobed plant cells. *Plant Physiol* 171: 2331-2342
- Zhang C, Halsey LE, Szymanski DB (2011) The development and geometry of shape change in *Arabidopsis thaliana* cotyledon pavement cells. *BMC Plant Biol* 11: 27

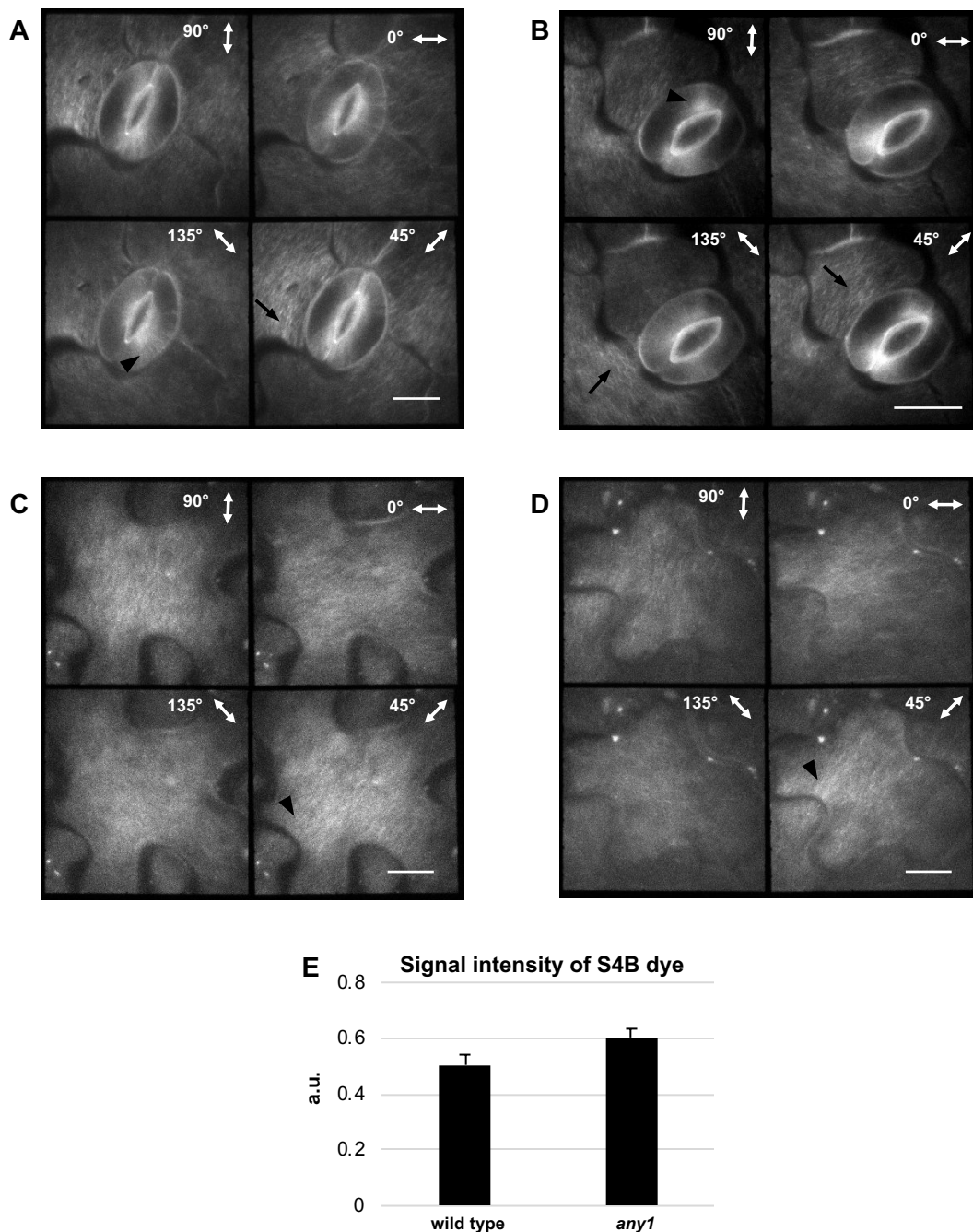


Fig. S3. Fluorescence polarization of S4B dye reflects the anisotropy degree of cellulose. A and B, Polarized fluorescence signals in guard cells and surrounding pavement cells in the Arabidopsis wild type at 3 days after germination stained with S4B. In A and B, the four images represent the polarization orientations at 0°, 45°, 90° and 135°. The polarized S4B signal indicated microfibrils to be arranged in radial orientation in the guard cells (arrowheads). This pattern is consistent with the documented orientation of cellulose microfibrils in this cell type (Fujita and Wasteneys, 2014). Moreover, S4B labeled cellulose microfibrils have a circular orientation in the pavement cells surrounding the guard cells (arrows), consistent with the orientation of cortical microtubules and stress patterns demonstrated previously (Sampathkumar et al., 2014). These results indicate that S4B molecules bind to cellulose microfibrils and can be used as a proxy to determine their alignment. C and D, Fluorescence polarization orientation of cellulose microfibrils stained with S4B, obtained from four images with different polarization orientations at 3 days after germination of wild type pavement cells. Arrows indicate instances of predominantly perpendicular alignment of cellulose to the neck side of the undulation. Scale bars = 10 μ m. E, Signal intensity of S4B dye staining cellulose at the neck region of wild type and *any1* mutant pavement cells. Error bars represent standard errors. N = 54 necks and adjacent lobes of the same undulation

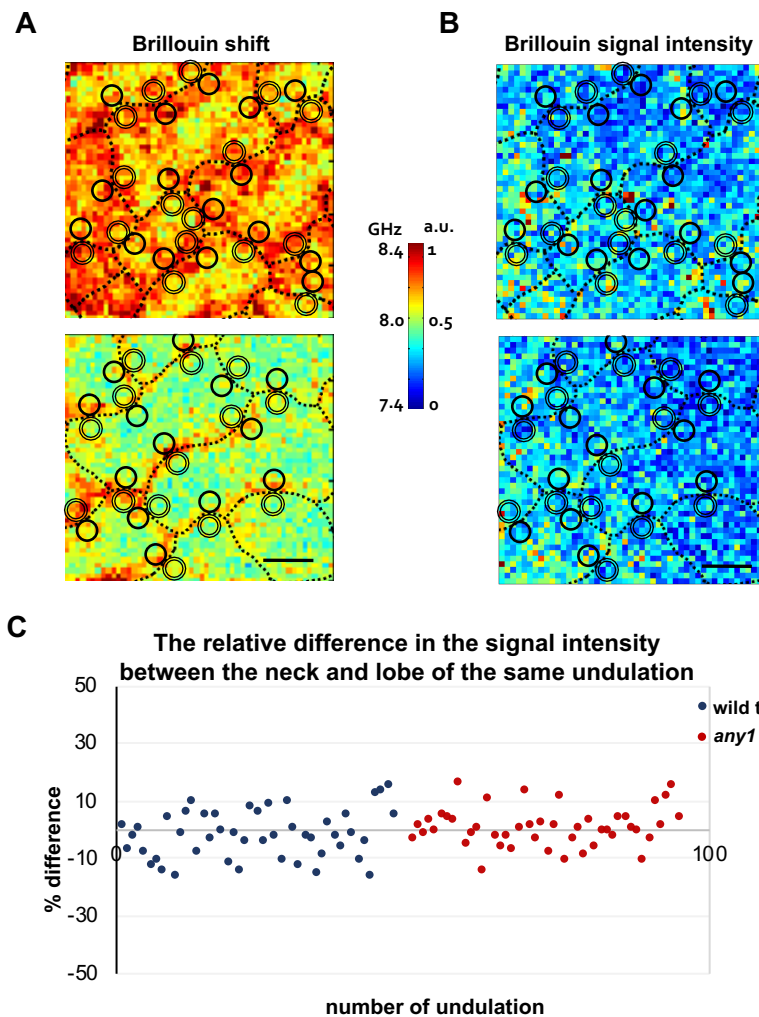
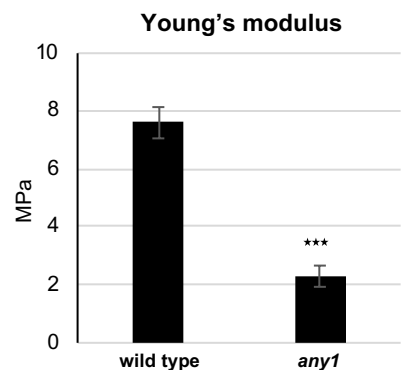


Fig. S4. Effect of pavement cell geometry on Brillouin signal intensity and Brillouin frequency shift. A and B, Brillouin shift (left panel) and Brillouin signal intensity (right panel) of wild type (A) and *any1* mutant (B) pavement cells at 1 day after germination. The Brillouin shift is given in GHz and is an indicator for the stiffness of the cell wall. Brillouin signal intensity is given in arbitrary unit (a.u.) and represents the amount of the reflected Brillouin shifts. In the micrographs, the dotted lines indicate cell outlines. Double lined circles (lobe region) and solid lined circles (neck region) indicate examples of ROIs used in C. Scale bars = 10 μ m. C, Distribution of the relative differences in the Brillouin signal intensity between the neck and the corresponding lobe of the same undulation. The relative difference was calculated as (signal intensity at neck region – signal intensity at lobe region) / (signal intensity at lobe region). The data represent the same undulations that are used to generate Fig. 3 C and D.

Fig. S5. Apparent Young's modulus of hypocotyls measured using tensile test. Hypocotyls of plasmolyzed dark-grown wild type and *any1* seedlings at 5 days after germination were tested. Asterisks indicate statistically significant differences compared to the wild type ($P < 0.001$, student's *t*-test). Error bars represent standard errors. N = 15 - 17 hypocotyls for each measurement.



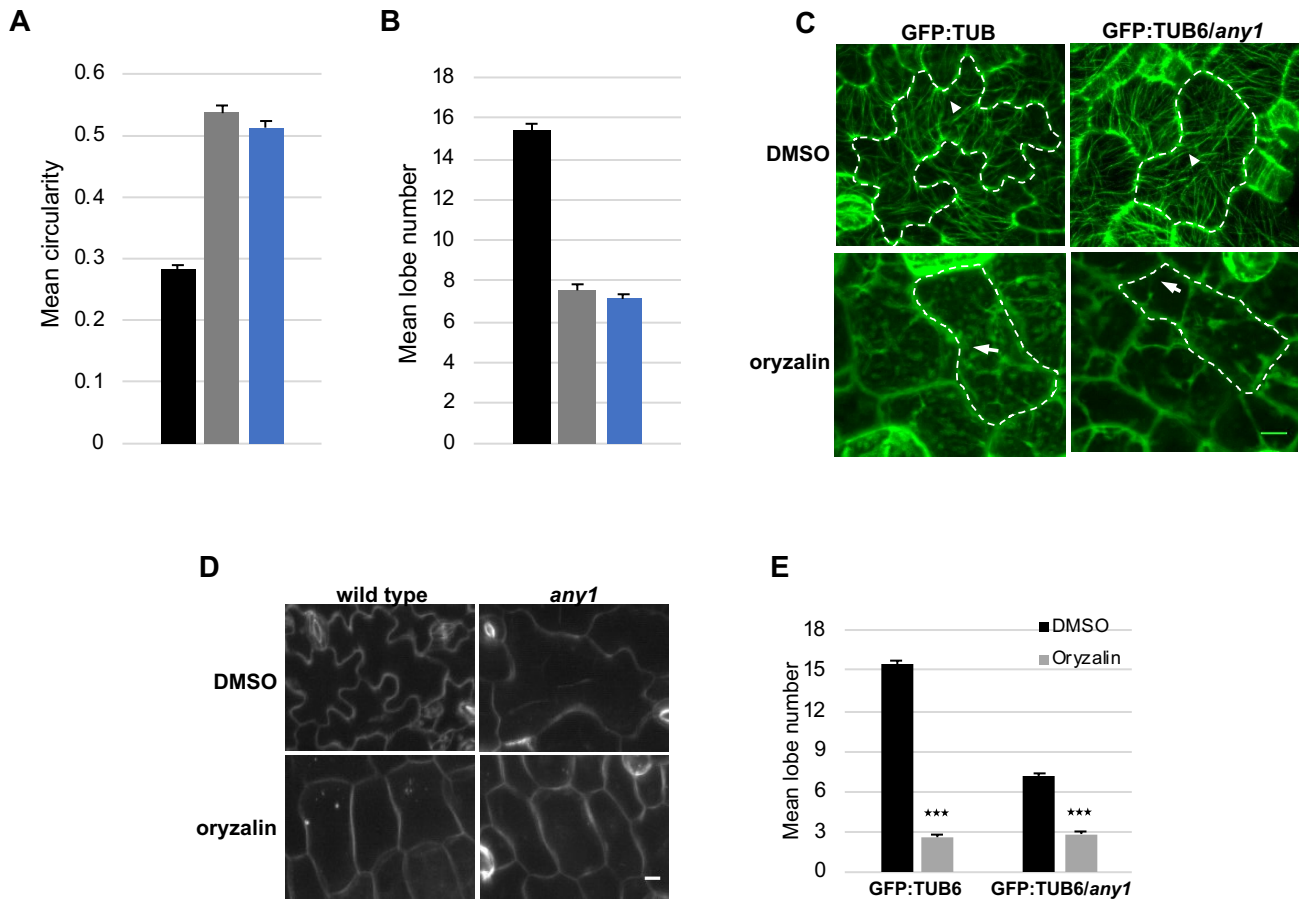


Fig. S6. Shape analysis of GFP:TUB6 and GFP:TUB6/*any1* pavement cells. A and B, Changes in mean circularity (A) and lobe number per cell (B) of GFP:TUB6 (black bars), *any1* (gray bars) and GFP:TUB6/*any1* (blue bars) pavement cells at 4 days after germination. Error bars represent the standard error. N = 40 cell from 6 seedlings for each measurement. C, Cortical microtubules in GFP:TUB6 (left panel) and GFP:TUB6/*any1* (right panel) pavement cells in DMSO (control; upper panel) and oryzalin (lower panel) treated cells. In the micrographs, the dashed lines indicate cell outlines. Arrowheads indicate instances of presence of cortical microtubules at the neck side of the undulation. Arrows indicate instances of absence of cortical microtubules at the neck side of the undulation. Brightness and contrast adjustments were done to ensure optimal contrast of microtubules on the presented micrographs. D, Effect of oryzalin treatment (lower panel) on the shape of pavement cells in wild type (left panel) and *any1* (right panel) compared to the control treatment (DMSO; upper panel). E, Mean number of lobes per cell in wild type and *any1* pavement cells in oryzalin (treatment) and DMSO (control). Error bars represent standard error. N = 35 cells from 6 different cotyledons. Asterisks indicate statistically significant differences between the DMSO control and the oryzalin treatment ($P < 0.001$, student's *t*-test). Scale bars = 10 μ m.

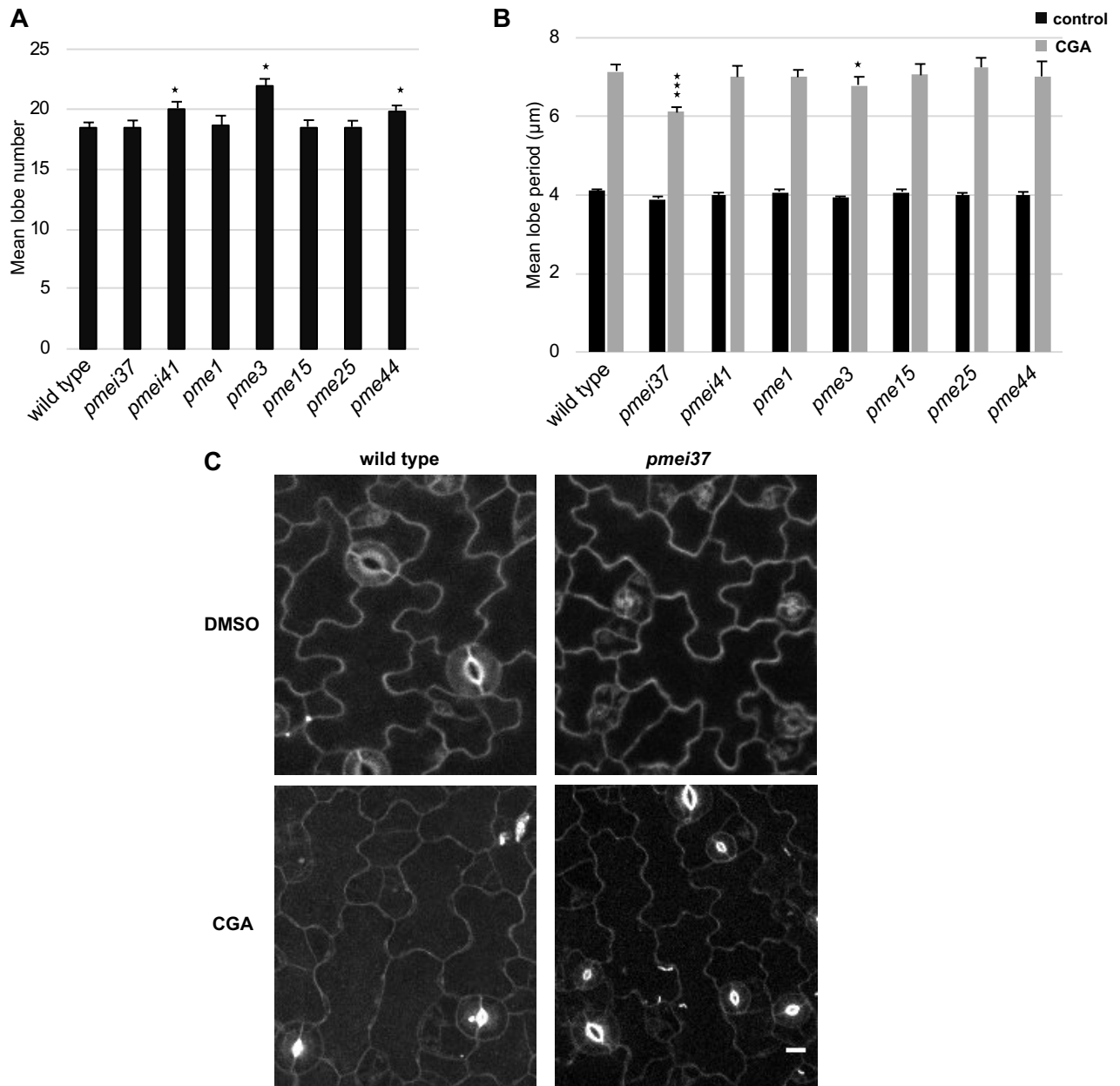


Fig. S7. Shape analysis of Arabidopsis wild type, PME and PME1 mutant pavement cells. A, Mean lobe number per cell of the wild type and *pme* and *pmei* mutant pavement cells at 4 days after germination. Asterisks indicate statistically significant differences compared to the wild type ($0.01 < P < 0.05$, student's *t*-test). B, Mean lobe period of the wild type and PME and PME1 mutants at 4 days after germination for control (black) and seedlings grown in the presence of CGA (grey). Lobe period equals square root convex hull area divided by number of lobes per cell. Asterisks in B indicate statistically significant differences compared to the wild type of the same treatment (* for $P < 0.05$ and *** for $P < 0.001$, student's *t*-test). Error bars in A and B represent standard error. $70 > N > 50$ cells from 10 to 15 seedlings for each measurement. C, Effect of CGA treatment (lower panel) on the shape of pavement cells in wild type (left panel) and *pmei37* (right panel) compared to the control treatment (DMSO; upper panel). Scale bar = 10 μm .

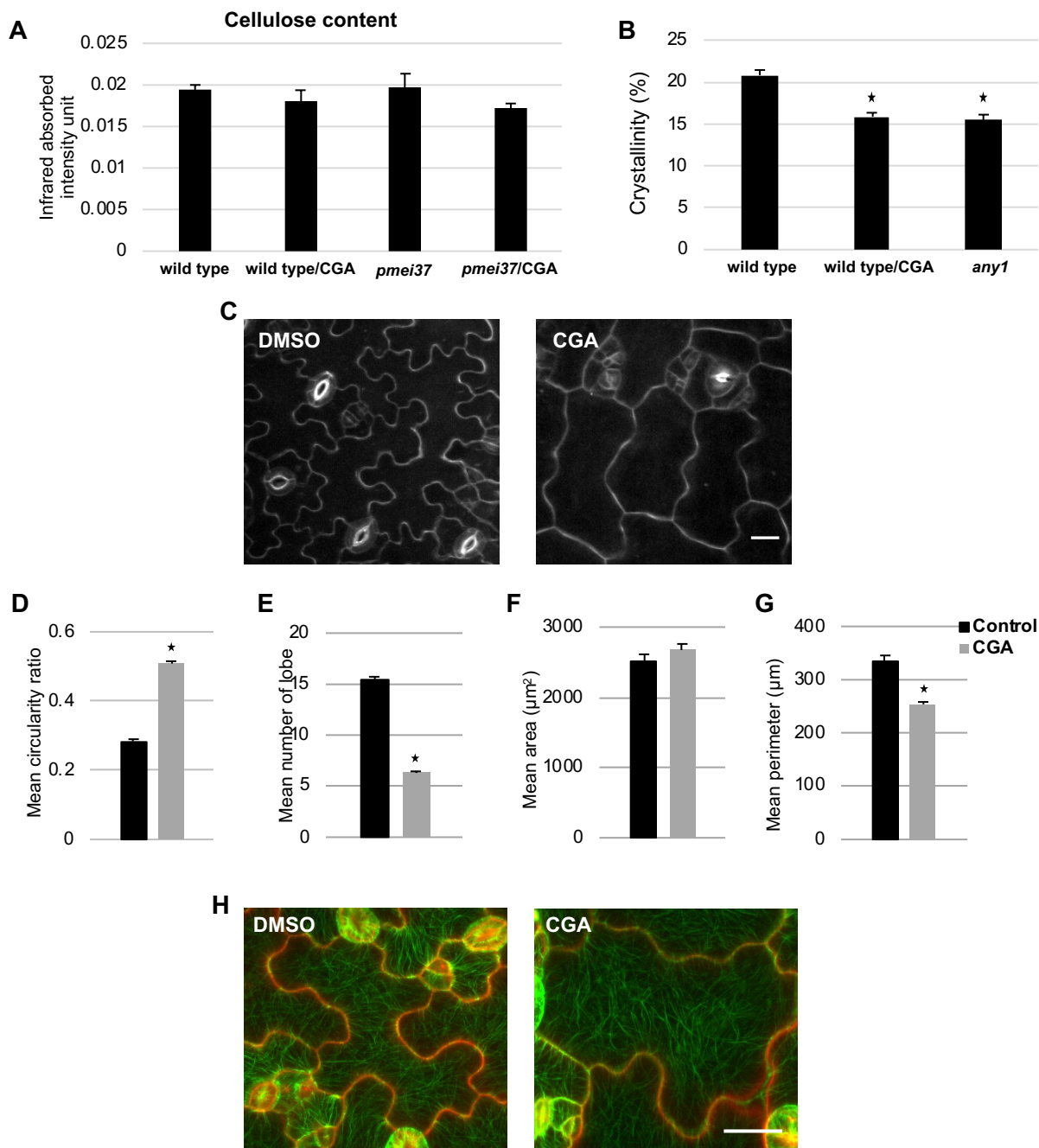


Fig. S8. Cellulose content and shape analysis of pavement cells under CGA treatment. A, Cellulose content in the wildtype and *pmei37* seedlings 4 days after germination under control and 0.9 nM CGA treatment determined using Attenuated Total Reflection spectroscopy. B, Degree of cellulose crystallinity in the cotyledons of wildtype seedlings 4 days after germination in presence of DMSO (control) and 0.9 nM CGA and in *any1* mutant using X-ray diffractometer. Error bars in A and B represent the standard error. Asterisks indicate statistically significant differences compared to the wild type ($P < 0.05$, student's *t*-test). Each bar represents data from 3 measurements, each measurement is a pool of 3 – 5 cotyledons. C, Fluorescence micrographs of pavement cells on the abaxial side of a cotyledon at 4 days after germination of wildtype grown in presence of DMSO (control) and 0.9 nM CGA (treatment), stained with propidium iodide. D to G, Mean circularity (D), number of true lobes per cell (E), cell area (F) and cell perimeter (G) at 4 days after germination of wild type pavement cells treated with 0.9 nM CGA (gray bars) and control cells (treated with DMSO; black bars). Error bars represent the standard error. Asterisks indicate statistically significant differences ($P < 0.001$, student's *t*-test). $N = 40 - 60$ cell from 8 - 10 seedlings for each measurement in D-G. H, Fluorescence micrographs of GFP:TUB6 pavement cells show cortical microtubules (green color) and cell wall (red color, stained with propidium iodide) grown in presence of DMSO (control) and 0.9 nM CGA (treatment). Scale bars = 20 µm.

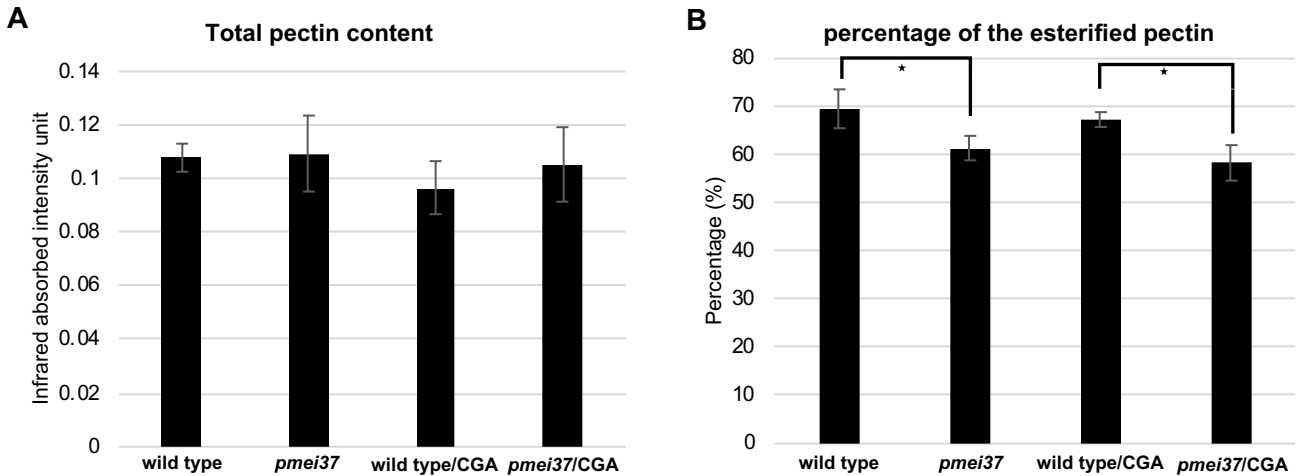


Fig. S9. Pectin content and percentage of esterified pectin in wild type and *pmei37* obtained using attenuated total reflection spectroscopy. A and B, Total pectin content (A) and percentage of esterified pectin (B) in the wildtype and *pmei37* seedlings 4 days after germination under control and 0.9 nM CGA treatment obtained using Attenuated Total Reflection spectroscopy. Asterisks indicate statistically significant differences ($0.01 < P < 0.05$, student's *t*-test). Error bars represent standard error. $4 < N < 7$ measurements, each measurement is a pool of 3 – 5 cotyledons.

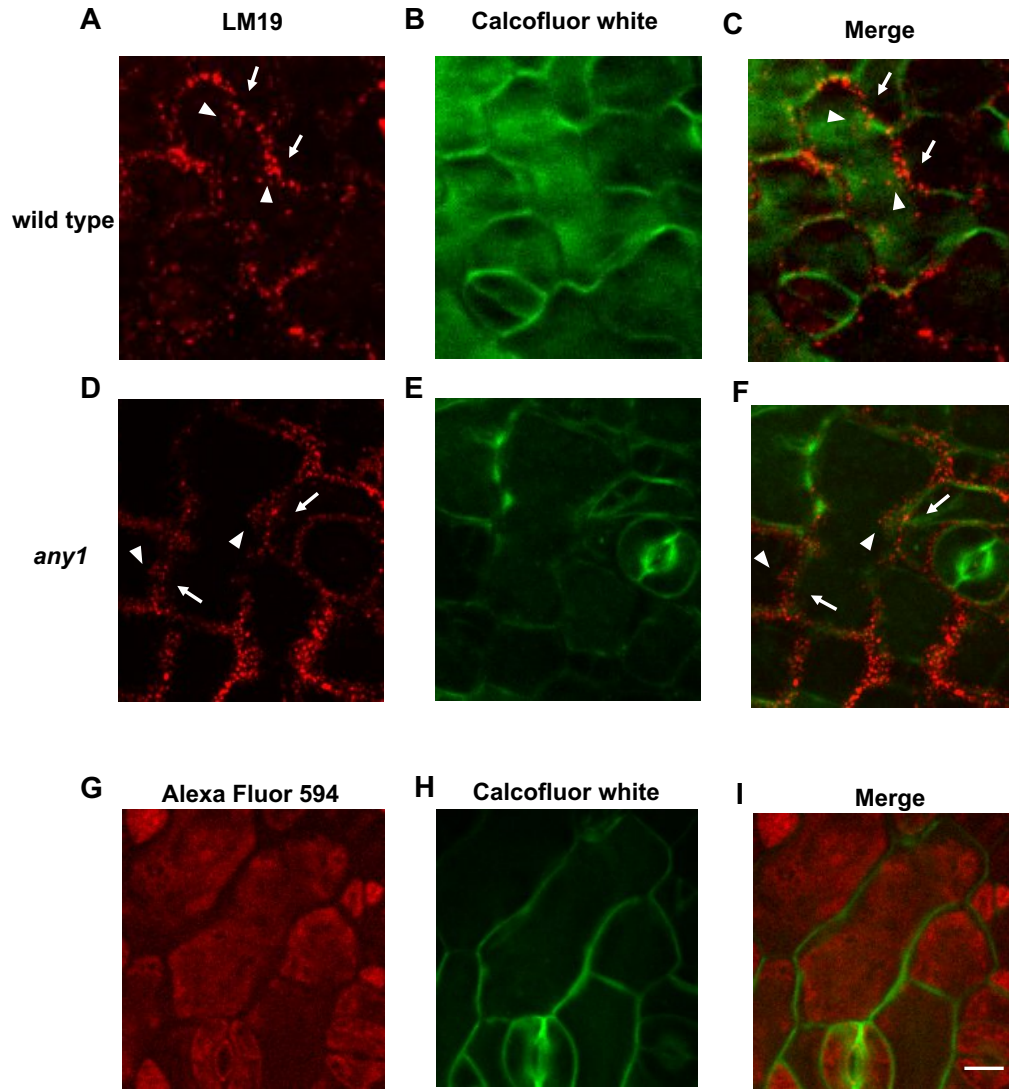


Fig. S10. Spatial arrangement of demethyl-esterified pectin in pavement cells of wild type and *any1* revealed by monoclonal antibody label. A and D, Maximum projections of z-stack images of pavement cells labeled with LM19 for demethyl-esterified pectin. B and E, Calcofluor white label (presenting cell shape). C and F, Merge of the LM19 and the calcofluor white fluorescence micrographs of wild type (A, B and C) and *any1* mutant (D, E and F). Arrowhead (neck region) and arrow (lobe region) indicate instances of high and low abundance of demethyl-esterified pectin at the neck and lobe regions, respectively. G, Maximum projections of z-stack of pavement cells stained only with Alexa Fluor 594, negative control for (A) and (D). H, Calcofluor white label (presenting cell shape in G). I, Merge of Alexa Fluor 594 and the calcofluor white micrographs. Scale bar = 10 μ m.

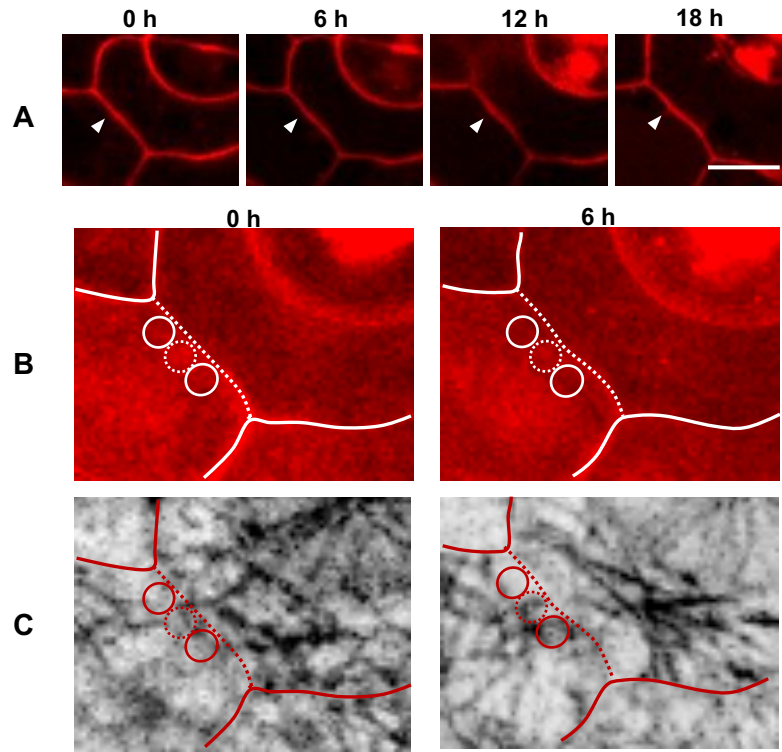


Fig. S11. Image analysis of pectin and microtubule dynamics during time lapse monitoring. Fluorescence micrographs of wildtype pavement cells were monitored over 18h and visualized in 6h time-lapse intervals. To correlate the dynamics of demethyl-esterified pectin and cortical microtubules with developing cell border curvatures, the fluorescence intensity was measured at the future border undulation and compared with that in adjacent regions. A, Single optical sections showing the anticlinal wall stained with propidium iodide over time. Arrowheads indicate the location on the cell border monitored over time in B and C. The prospective curvature of the straight line at time 0 was selected based on the curvature at 18h. B and C, Maximum projections of z-stacks of same sample as in A, at 0h and 6h, showing propidium iodide signal for demethyl-esterified pectin (B) and cortical microtubules at the periclinal wall (GFP:TUB6) (C). Dotted circles in B and C indicate tip of the prospective neck region (region of interest). Solid line circles represent adjacent regions. The signal intensity of the dotted ROI was divided by the mean intensity signal of the two adjacent solid line ROIs in order to obtain the relative intensity difference. White and red lines in B and C show the anticlinal wall that is shown in A. The dotted regions of the white and red lines in B and C represents the anticlinal wall of interest. Scale bars = 10 μ m.